JACS
JOURNAL OF THE AMERICAN CHEMICAL SOCIETY

COMMUNICATION

pubs.acs.org/JACS

Shape- and Size-Controlled Synthesis in Hard Templates: Sophisticated Chemical Reduction for Mesoporous Monocrystalline Platinum Nanoparticles

Hongjing Wang,[†,‡] Hu Young Jeong,[§] Masataka Imura,[†] Liang Wang,[†] Logudurai Radhakrishnan,[†] Nobuhisa Fujita,[∥] Toen Castle,[⊥] Osamu Terasaki,[§,⊥] and Yusuke Yamauchi[†,‡,#,*]

[†]World Premier International (WPI) Research Center for Materials Nanoarchitectonics (MANA), National Institute for Materials Science (NIMS), 1-1 Namiki, Tsukuba, Ibaraki 305-0044, Japan

[‡]Faculty of Science and Engineering, Waseda University, 3-4-1 Okubo, Shinjuku, Tokyo 169-8555, Japan

[§]Graduate School of EEWS, WCU Energy Science and Engineering, KAIST, Daejeon 305-701, Korea

[∥]Institute of Multidisciplinary Research for Advanced Materials (IMRAM), Tohoku University, Katahira 2-1-1, Aoba, Sendai 980-8577, Japan

[⊥]Inorganic and Structural Chemistry, Arrhenius Laboratory, Stockholm University, 10691 Stockholm, Sweden

[#]Precursory Research for Embryonic Science and Technology (PRESTO), Japan Science and Technology Agency (JST), 4-1-8 Honcho, Kawaguchi, Saitama 332-0012, Japan

Supporting Information

ABSTRACT: Here we report a novel hard-templating strategy for the synthesis of mesoporous monocrystalline Pt nanoparticles (NPs) with uniform shapes and sizes. Mesoporous Pt NPs were successfully prepared through controlled chemical reduction using ascorbic acid by employing 3D bicontinuous mesoporous silica (KIT-6) and 2D mesoporous silica (SBA-15) as a hard template. The particle size could be controlled by changing the reduction time. Interestingly, the Pt replicas prepared from KIT-6 showed polyhedral morphology. The single crystallinity of the Pt fcc structure coherently extended over the whole particle.

Since the discovery of mesoporous materials in the early 1990s,[1] various types of ordered mesoporous materials have been synthesized under different conditions and extensively studied with regard to mesostructural controllability, compositional diversity, and morphological flexibility.[2] Currently, mesoporous silica[3] and carbon[4] nanoparticles (NPs) with controlled particle size have attracted great interest in many potential applications of chromatography, catalysis, catalyst support, and adsorption because the NPs can provide outstanding pore accessibility of guest species from outside. Especially, mesoporous NPs below submicrometer size (normally, below 500 nm) can be utilized in biomedical applications.[5] To date, many efforts have been made in the synthesis of mesoporous NPs.

In comparison with silica and carbon, mesoporous metals have fascinating properties inherent to metal frameworks (e.g., high electroconductivity, catalytic activities, etc.) along with the general characteristics of mesoporous materials.[6] Therefore, we can anticipate various electrochemical applications that cannot be realized by traditional mesoporous silica. Several approaches for the preparation of mesoporous/mesostructured metals have been reported. Lyotropic liquid crystals made of highly concentrated surfactants or block copolymers have been utilized as soft templates.[7] Through chemical or electrochemical reduction, ordered mesoporous metal powders or films, respectively, can be synthesized. However, the ordered arrangement of the rod self-assemblies in the liquid crystals is often distorted during the metal deposition process, and thus, long-range order of the mesoporous structures in the final product is lacking.[8] In comparison with the soft-templating method, hard templating is a very attractive pathway that is widely applicable to various compositions.[9] Mesoporous silica with a robust framework and high thermal stability is used as a hard template to synthesize a metal replica.[10] To date, various Pt nanostructures such as 1D nanowires and 3D nanowire networks have been prepared by using MCM-41 (*p6mm*), SBA-15 (*p6mm*), KIT-6 ($Ia\bar{3}d$), and MCM-48 ($Ia\bar{3}d$) as hard templates.[10] Chao and co-workers[11] used transmission electron microscopy (TEM) to investigate the growth mechanism of Pt nanostructures in mesoporous silica matrixes (MCM-48 and MCM-41).

Despite these recent advances in soft and hard templates, the obtained morphologies of *mesoporous metals* have been very limited to only powders with irregular morphology or films on conductive substrates. The lack of control over the particle sizes and morphologies is a serious problem for further development of mesoporous metals. The shape and size distribution of the NPs are critical parameters of the function and utility for applications. To bring out shape- and size-dependent physicochemical properties, it is extremely important to prepare uniform-sized particles with the same shapes in high yields.

In this communication, we propose a new concept for the shape- and size-controlled synthesis of mesoporous metals in hard templates. We demonstrate the facile synthesis of uniformly sized mesoporous Pt NPs by using mesoporous silica KIT-6 ($Ia\bar{3}d$) and SBA-15 (*p6mm*) as the hard template [Figure S1 in the Supporting Information (SI)] and ascorbic acid (AA) as the reducing agent. The unit cell parameters and mesopore sizes of

Received: June 23, 2011
Published: August 30, 2011

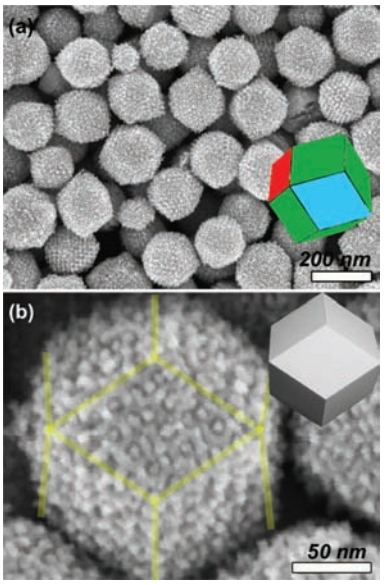

Figure 1. (a) Low- and (b) high-magnification SEM images of the obtained mesoporous Pt nanoparticles (*meso*-Pt) prepared with mesoporous silica KIT-6. An enlargement of (a) is shown in Figure S2.

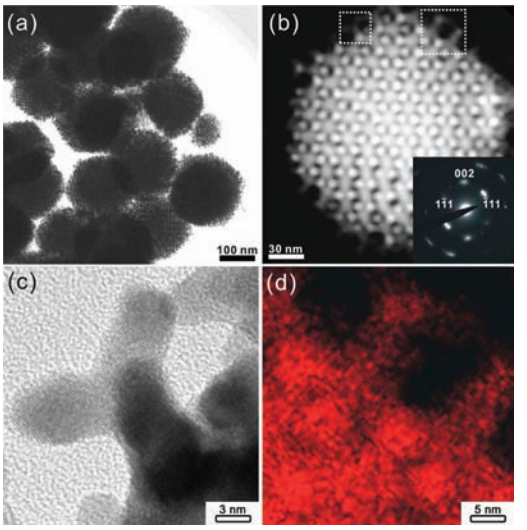

Figure 2. (a) Low-magnification TEM image of *meso*-Pt prepared using KIT-6. (b) ADF-STEM image of one *meso*-Pt. The inset shows an ED pattern taken from this particle using an incident beam direction parallel to [110] of the Pt fcc structure. (c) High-magnification TEM image taken at the left square box in (b). (d) Energy-dispersive spectroscopy elemental (Pt) mapping obtained at the right square box in (b).

the original templates were 21 and 7.9 nm for KIT-6 and 9.2 and 7.3 nm for SBA-15, respectively. Details are given in the SI.

First, mesoporous silica powders were immersed into an aqueous solution of K_2PtCl_4. Next, the composites were dried under reduced vacuum conditions, giving an orange powder. Aqueous AA as a reducing agent was dropped on the powder. After 12 h, the sample color had totally changed from orange to black, giving a product hereafter called the *meso*-Pt/silica composite. Finally, to remove the silica, the black powder was washed with HF solution to give mesoporous Pt (*meso*-Pt). All of the experiments were carried out at room temperature.

Figure 1 shows the morphology of the obtained *meso*-Pt after the removal of the silica template (an enlarged image is shown in Figure S2). The low-magnification scanning electron microscopy (SEM) image confirmed that the NPs were isolated from each other and had a narrow particle size distribution. Interestingly, almost all of the NPs showed rhombic dodecahedral morphology (as indicated by the yellow lines in Figure 1b), although some appeared to be different in the SEM images because different projections were viewed (Figure S3). The external surface was bounded by 12 planes. The crystal morphology was commensurate with cubic $m\bar{3}m$ point-group symmetry.

From high-magnification SEM images (Figure 1b and Figure S3b), it was observed that Pt nanowires replicated from both side pores of a double gyroid mesostructure (i.e., inverse double gyroid structure). Also, the small-angle X-ray scattering (SAXS) peaks were assignable to $Ia\bar{3}d$, giving the same SAXS profile as for the original KIT-6 mesoporous silica (Figure S4a). This is evidence that the replication of Pt from KIT-6 retained the original symmetry. However, a very weak 110 reflection that was not observed in the profile of the original KIT-6 appeared in the SAXS pattern of *meso*-Pt/silica (Figure S4a), meaning that formation of a lower-symmetry material partially takes place at this stage. This results from Pt deposition occurring in one side pores of the bicontinuous structure, as indicated by the dotted ellipse in Figure S2.

The N_2 adsorption−desorption isotherm of *meso*-Pt was a typical type-IV isotherm (Figure S5b), characteristic of mesoporous materials. The BET surface area and BJH average pore size were calculated to be 39.0 m^2/g and 2.7 nm, respectively. The mesopore size of 2.7 nm indicates void space between the Pt nanowires. This value is in good agreement with the wall thickness of the original KIT-6. TEM images and the elemental mapping are displayed in Figure 2. The annular dark-field scanning TEM (ADF-STEM) image of one *meso*-Pt (Figure 2b) is well-consistent with the image of the original KIT-6 ($Ia\bar{3}d$ space group) taken with the incident beam parallel to the ⟨111⟩ direction. Thus, *meso*-Pt corresponds to a perfect inversion replica of the original highly ordered KIT-6. Notably, the electron diffraction (ED) pattern (Figure 2b inset) taken from this same particle showed that the Pt within the framework possessed an almost single-crystalline nature of the Pt face-centered cubic (fcc) structure. The wide-angle X-ray diffraction (WAXRD) pattern of *meso*-Pt could also be assigned to the Pt fcc crystal structure (Figure S6).

To understand the Pt deposition process, several types of *meso*-Pt with different particle sizes were prepared by changing the reduction time (10 min, 1 h, and 12 h) (Figures S7 and S8). When the reduction time was 10 min, the deposited Pt particles showed a polyhedral shape with an average diameter of 80 nm (Figures S7a and S8a). With an increase in the deposition period to 1 h, the average particle size gradually increased (up to 160 nm) with retention of the polyhedral shape (Figures S7b and S8b). After the complete reduction of the Pt sources (12 h), the average particle size reached 180 nm (Figure 1 and Figure S8c). On the basis of these results, at the beginning stage of the Pt deposition, the nucleation occurs at the center of the particles. Next, Pt grain growth from the nuclei increasingly proceeds, forming larger-sized particles, while coherently retaining the Pt atomic crystallinity over the full region of each particle, as shown in Figure 2b,c.

With the increase in particle size, the single-domain size of the "mesoporous crystals" became large. Actually, the intensities of the SAXS profiles increased and the full width at half-maximum (fwhm) decreased (Figure S9). Similarly, the WAXRD patterns

(Figure S6) also showed the increase in peak intensities and decrease in fwhm, indicating the enlargement of Pt fcc crystal domains with increasing particle size.

To clarify the reason why each particle shows a "single mesoporous crystal", the *meso*-Pt/silica composites before the silica removal were carefully investigated by TEM. The deposited Pt particles were distributed over the entire of the silica matrix and isolated from each other. As clearly seen in Figure S10, the Pt particles were deposited within the same single mesostructural $Ia\bar{3}d$ domain of the original KIT-6. The domain sizes of "mesoporous crystals" with the same orientation in the KIT-6 template were submicrometer scale (Figure S11), which is much larger than the particle sizes of the deposited *meso*-Pt particles. Therefore, it is very reasonable that the obtained Pt particles were single mesoporous crystals without defects (Figure 2b).

The strength of the reducing agent plays the most important key role in the successful preparation of mesoporous Pt nanoparticles with uniform size. For comparison, two different kinds of reducing agents, sodium borohydride (SBH) and dimethylaminoborane (DMAB), were used instead of AA. In both cases, the deposited Pt showed irregular morphology (Figure S12). Some particles had no ordered mesoporous structures as a result of Pt deposition on the outer surface of the mesoporous silica. The peak intensities in the low-angle range were much smaller than for *meso*-Pt obtained using AA (Figure S13), exactly consistent with the SEM images. These results prove that the use of AA is vital for formation of Pt polyhedra with well-ordered mesostructures. The Pt deposition rate is determined by the strength of the reducing agent. The redox potentials of SBH and DMAB are much lower than that of AA. Therefore, relative to AA, SBH and DMAB are very strong reducing agents and can reduce Pt sources very rapidly. Therefore, SBH and DMAB molecules cannot enter the mesopores and reduce the Pt species inside the mesoporous particles. Especially, SBH reduced the Pt species immediately by a very severe self-decomposition reaction with a large volume of gas, thereby depositing the Pt outside the mesoporous particles (Figure S14). In contrast, the use of AA can provide enough time to access the Pt sources located inside the mesopores (Figure S10). In the initial stage of Pt deposition, the AA reduced the Pt species embedded inside the mesopores to deposit the Pt nuclei, and the grain growth proceeded continuously from the primary Pt nuclei. Consequently, the reaction kinetics was critical for high-quality synthesis.

In general, fcc metals such as Pt and Au normally have minimum surface energy for {111}, which is the reason for the formation of typical mutiply twinned structures.[12] However, we could not observe such a special crystallographic surface on the top of the Pt network (Figure 1 and Figure S2). In a careful TEM investigation (Figure 3 and Table S1), we could not find any special crystallographic orientation relationship between the KIT-6 mesostructure ($Ia\bar{3}d$) and the Pt fcc structure ($Fm\bar{3}m$), although the atomic coherency of the Pt crystal in *meso*-Pt was confirmed (Figures 2b and 3). It is therefore natural to assume that the rhombic-dodecahedral shape of the Pt replica synthesized from KIT-6 is not an equilibrium form reflecting the crystal morphology of the Pt fcc structure but originates from the KIT-6 mesostructure, that is, the geometry of the double gyroid channels ($Ia\bar{3}d$ symmetry).

From the viewpoint of the electrochemical process, Pt nucleation on the silica walls of KIT-6 is thought to be less than Pt grain growth from the Pt nuclei. In other words, after the nuclei are formed in the early stage of the reaction, most of the reaction time

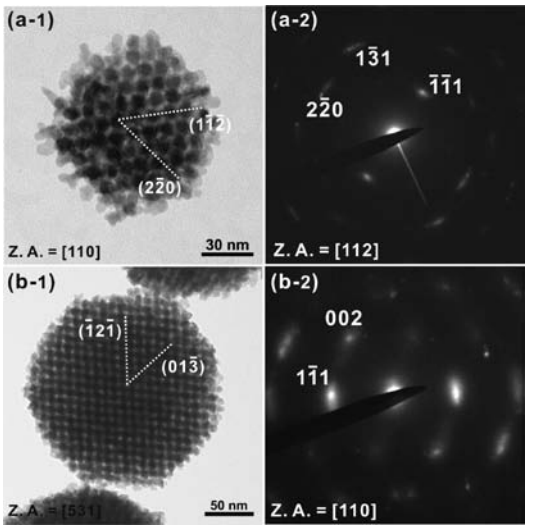

Figure 3. (a-1, b-1) Low-magnification bright-field TEM images of *meso*-Pt and (a-2, b-2) the corresponding ED patterns. Indices are based on (a-1, b-1) the KIT-6 mesostructure and (a-2, b-2) Pt fcc.

is spent for the growth process. This idea is nicely supported by the fact that (i) the density of the Pt particles (i.e., the number of Pt particles per unit area) was almost constant irrespective of the reaction time (Figure S10) and (ii) the particle size gradually increased with the reaction time (Figures S7 and S8). Furthermore, coalescence of the particles was not confirmed (Figure S2). Thus, interference among Pt particles to produce their aggregation was rather small. If the density of the nucleation sites were larger, such interference would become relatively large, which would tend to cause the condition of "partition of the space". In this case, Pt ions diffusing from the associated space to each nucleus (i.e., the Voronoi cell) are likely to contribute to the growth of the Pt particle. The envelope surface must therefore reflect the shape of the Voronoi cell.

In order to discuss further the present formation mechanism, let us assume that the diffusion of the Pt sources as well as that of the reducing agent is fast enough that it would not limit the deposition rate of Pt at every growth front. The Pt network would then grow by tracing the channels of the KIT-6 template outward from the nucleation center with a uniform speed. Figure S15 illustrates an early snapshot of the Pt network, assuming the nucleation center is a single ternary junction of the gyroid network. At a later stage, the Pt network would exhibit a polyhedral envelope with 24 triangular faces (Figure S15b). This shape is related to the rhombic dodecahedron observed experimentally, as shown in Figure 1.

This slight discrepancy may be caused by a bias of the supply of Pt sources along certain directions in the $Ia\bar{3}d$ channel network. The double gyroid channels in KIT-6 are formed by connections between the branched points that correspond to Wyckoff 16b positions (site symmetry = 32) for $Ia\bar{3}d$. As shown in Figure S16, the gyroidal channels are orthogonal to the {110} faces of the cubic structure. The formation of rhombic dodecahedra in this study might indicate that the supply of Pt ions and AA can be topologically delayed along the normal to the {110} planes.

Our synthetic concept reported here was also applied to a different Pt replica system using mesoporous silica SBA-15. After the silica removal, highly ordered mesoporous Pt NPs with an olive shape were formed (Figure S17). The Pt NPs obtained from SBA-15 showed olivelike morphology with an average

length of around 200 nm. On the NPs surface, it was observed that the several Pt nanowires were periodically arranged, forming a negative replica of the 2D hexagonally ordered mesoporous silica. The SAXS patterns (Figure S4b) before and after the silica removal showed typical peaks assignable to the 10, 11, and 20 planes of a 2D hexagonal symmetry. The Pt replicas prepared from SBA-15 also possessed the single-crystalline nature of Pt fcc (Figure S18). The surface area and average pore size were calculated to be 37.0 m^2/g and 3.2 nm, respectively (Figure S5d). The mesopore size of 3.2 nm indicates void space enclosed by four Pt nanowires. This value is in good agreement with the wall thickness of the original mesoporous silica SBA-15.

In order to investigate its potential as a catalytic electrode, we measured the methanol electrochemical oxidation reaction on *meso*-Pt replicated from KIT-6. The electrocatalytic performance recorded in an aqueous solution containing methanol is displayed in Figure S19. As shown in Figure S19a, two visible anodic peaks occurring on the positive and negative sweeps, which are typical features of the methanol oxidation process, were confirmed. It is quite interesting that small-sized *meso*-Pt (deposited for 10 min) showed a remarkably large current density for the electrocatalytic methanol oxidation, in comparison to *meso*-Pt with larger sizes (deposited for 1 h and 12 h) and commercially available Pt black catalyst (Figure S19d). In comparison with commercially available Pt catalysts, the onset potentials of *meso*-Pt were clearly negatively shifted (Figure S19b). Chronoamperometric curves recorded at 0.6 V proved that small-sized *meso*-Pt exhibited high durability in its catalytic performance (Figure S19c). The above results revealed that using small-sized *meso*-Pt allowed the methanol molecules to access all of the inner mesopores more easily without serious diffusion resistance. Although 3D-connected mesopores are generally known to make the entire surface readily accessible by reactants, the small-sized *meso*-Pt can more effectively supply the reactants into the mesopores.

In conclusion, we have successfully synthesized monodispersed polyhedral- and olive-shaped mesoporous Pt nanoparticles with uniform particle sizes by using KIT-6 and SBA-15, respectively, as templates. The yield in the present work reached ~97%, although very few Pt sources were lost in the centrifuging and washing processes. Almost all of the Pt sources were impregnated into the entire mesopore space and reduced inside the hard templates without Pt bulk deposition outside the mesopores. The present reduction process without high temperature and complex equipment is very simple and highly reproducible, which will be useful for large-scale production in the future. We strongly believe that this method provides a generic platform for the preparation of mesoporous metal NPs that can be used for other metal compositions. Well-defined morphology and uniformity in size (Figure S8) will become very important aspects for the future use of mesoporous metals in a wide range of applications such as electrodes, sensors, catalysis, and drug delivery.

■ ASSOCIATED CONTENT

Supporting Information. Details of the synthetic method and characterization data. This material is available free of charge via the Internet at http://pubs.acs.org.

■ AUTHOR INFORMATION

Corresponding Author
Yamauchi.Yusuke@nims.go.jp

■ REFERENCES

(1) (a) Yanagisawa, T.; Shimizu, T.; Kuroda, K.; Kato, C. *Bull. Chem. Soc. Jpn.* **1990**, *63*, 988. (b) Yanagisawa, T.; Shimizu, T.; Kuroda, K.; Kato, C. *Bull. Chem. Soc. Jpn.* **1990**, *63*, 1535. (c) Kresge, C. T.; Leonowicz, M. E.; Roth, W. J.; Vartuli, J. C.; Beck, J. S. *Nature* **1992**, *359*, 710.

(2) Wan, Y.; Zhao, D. *Chem. Rev.* **2007**, *107*, 2821.

(3) (a) Fowler, C. E.; Khushalani, D.; Lebeau, B.; Mann, S. *Adv. Mater.* **2001**, *13*, 649. (b) Kim, T. W.; Chung, P. W.; Lin, V. S. Y. *Chem. Mater.* **2010**, *22*, 5093. (c) Cauda, V.; Schlossbauer, A.; Kecht, J.; Zürner, A.; Bein, T. *J. Am. Chem. Soc.* **2009**, *131*, 11361. (d) Urata, C.; Yamada, H.; Wakabayashi, R.; Aoyama, Y.; Hirosawa, S.; Arai, S.; Takeoka, S.; Yamauchi, Y.; Kuroda, K. *J. Am. Chem. Soc.* **2011**, *133*, 8102. (e) Suteewong, T.; Sai, H.; Lee, J.; Bradbury, M.; Hyeon, T.; Gruner, S. M.; Wiesner, U. *J. Mater. Chem.* **2010**, *20*, 7807. (f) Lee, J. E.; Lee, N.; Kim, H.; Kim, J.; Choi, S. H.; Kim, J. H.; Kim, T.; Song, I. C.; Park, S. P.; Moon, W. K.; Hyeon, T. *J. Am. Chem. Soc.* **2010**, *132*, 552. (g) Kim, J.; Lee, J. E.; Lee, J.; Yu, J. H.; Kim, B. C.; An, K.; Hwang, Y.; Shin, C. H.; Park, J. G.; Kim, J.; Hyeon, T. *J. Am. Chem. Soc.* **2006**, *128*, 688.

(4) (a) Fang, Y.; Gu, D.; Zou, Y.; Wu, Z.; Li, F.; Che, R.; Deng, Y.; Tu, B.; Zhao, D. *Angew. Chem., Int. Ed.* **2010**, *49*, 7987. (b) Kim, T. W.; Chung, P. W.; Slowing, I. I.; Tsunoda, M.; Yeung, E. S.; Lin, V. S. Y. *Nano Lett.* **2008**, *8*, 3724. (c) Gu, D.; Bongard, H.; Meng, Y.; Miyasaka, K.; Terasaki, O.; Zhang, F.; Deng, Y.; Wu, Z.; Feng, D.; Fang, Y.; Tu, B.; Schüth, F.; Zhao, D. *Chem. Mater.* **2010**, *22*, 4828.

(5) (a) Giri, S.; Trewyn, B. G.; Lin, V. S. Y. *Nanomedicine* **2007**, *2*, 99. (b) Slowing, I. I.; Wu, C. W.; Vivero-Escoto, J. L.; Lin, V. S. Y. *Small* **2009**, *5*, 57. (c) Lu, J.; Liong, M.; Li, Z.; Zink, J. I.; Tamanoi, F. *Small* **2010**, *6*, 1794.

(6) (a) Saramat, A.; Andersson, M.; Hant, S.; Thormahlen, P.; Skoglundh, M.; Attard, G. S.; Palmqvist, A. E. C. *Eur. Phys. J. D* **2007**, *43*, 209. (b) Yamauchi, Y.; Kuroda, K. *Chem.—Asian J.* **2008**, *3*, 664. (c) Saramat, A.; Thormahlen, P.; Skoglungh, M.; Attard, G. S.; Palmqvist, A. E. C. *J. Catal.* **2008**, *253*, 253.

(7) (a) Attard, G. S.; Goltner, C. G.; Corker, J. M.; Henke, S.; Templer, R. H. *Angew. Chem., Int. Ed. Engl.* **1997**, *36*, 1315. (b) Attard, G. S.; Bartlett, P. N.; Coleman, N. R. B.; Elliott, J. M.; Owen, J. R.; Wang, J. H. *Science* **1997**, *278*, 838. (c) Yamauchi, Y.; Takai, A.; Nagaura, T.; Inoue, S.; Kuroda, K. *J. Am. Chem. Soc.* **2008**, *130*, 5426. (d) Yamauchi, Y.; Sugiyama, A.; Morimoto, R.; Takai, A.; Kuroda, K. *Angew. Chem., Int. Ed.* **2008**, *47*, 5371. (e) Yamauchi, Y.; Komatsu, M.; Fuziwara, M.; Nemoto, Y.; Sato, K.; Yokoshima, T.; Sukegawa, H.; Inomata, K.; Kuroda, K. *Angew. Chem., Int. Ed.* **2009**, *48*, 7792.

(8) Bender, F.; Mankelow, R. K.; Hibbert, D. B.; Gooding, J. J. *Electroanalysis* **2006**, *18*, 1558.

(9) (a) Lee, J.; Yoon, S.; Hyeon, T.; Oh, S. M.; Kim, K. B. *Chem. Commum.* **1999**, 2177. (b) Ryoo, R.; Joo, S. H.; Jun, S. *J. Phys. Chem. B* **1999**, *103*, 7743. (c) Lee, J.; Yoon, S.; Oh, S. M.; Shin, C. H.; Hyeon, T. *Adv. Mater.* **2000**, *12*, 359. (d) Yoon, S.; Lee, J. W.; Hyeon, T.; Oh, S. M. *J. Electrochem. Soc.* **2000**, *147*, 2507. (e) Lee, J.; Kim, J.; Hyeon, T. *Chem. Commun.* **2003**, 1138. (f) Lu, A. H.; Schüth, F. *Adv. Mater.* **2006**, *18*, 1793. (g) Tüysüz, H.; Comotti, M.; Schüth, F. *Chem. Commun.* **2008**, 4022. (h) Rumplecker, A.; Kleitz, F.; Salabas, E. L.; Schüth, F. *Chem. Mater.* **2007**, *19*, 485. (i) *Nanocasting: A Versatile Strategy for Creating Nanostructured Porous Materials*; Lu, A. H., Zhao, D., Wan, Y., Eds.; RSC Publishing: Cambridge, U.K., 2006.

(10) (a) Shin, H. J.; Ryoo, R.; Liu, Z.; Terasaki, O. *J. Am. Chem. Soc.* **2001**, *123*, 1246. (b) Liu, Z.; Terasaki, O.; Ohsuna, T.; Hiraga, K.; Shin, H. J.; Ryoo, R. *ChemPhysChem* **2001**, *2*, 229. (c) Liu, Z.; Sakamoto, Y.; Ohsuna, T.; Hiraga, K.; Terasaki, O.; Ko, C. H.; Shin, H. J.; Ryoo, R. *Angew. Chem., Int. Ed.* **2000**, *39*, 3107. (d) Doi, Y.; Takai, A.; Sakamoto, Y.; Terasaki, O.; Yamauchi, Y.; Kuroda, K. *Chem. Commun.* **2010**, *46*, 6365.

(11) (a) Guo, X. J.; Yang, C. M.; Liu, P. H.; Cheng, M. H.; Chao, K. J. *Cryst. Growth Des.* **2005**, *5*, 33. (b) Chao, K. J.; Chang, Y. P.; Chen, Y. C.; Lo, A. S.; Phan, T. H. *J. Phys. Chem. B* **2006**, *110*, 1638.

(12) Lu, X.; Rycenga, M.; Skrabalak, S. E.; Wiley, B.; Xia, Y. *Annu. Rev. Phys. Chem.* **2009**, *60*, 167.